Homology Modeling of Gelatinase Catalytic Domains and Docking Simulations of Novel Sulfonamide Inhibitors

Ryuichi Kiyama, Yoshinori Tamura, Fumihiko Watanabe, Hiroshige Tsuzuki, Mitsuaki Ohtani, and Mitsuaki Yodo*

Shionogi Research Laboratories, Shionogi & Company, Ltd., Sagisu, Fukushima-ku, Osaka 553-0002, Japan

Received September 8, 1998

Three-dimensional models for the catalytic domain of gelatinases (MMP-9 and -2) have been constructed based on the X-ray crystal structure of MMP-3. Conformations of the loop segment which forms the bottom half of the S1′ subsite but shows conformational diversity among the crystal structures of other MMPs have been explored by simulated annealing of each gelatinase model complexed with two highly potent "probe" inhibitors. Representative catalytic domain models have been selected for each gelatinase from the set of generated conformations based on shape complementarity of the loop to the probe inhibitors. The single model selected for MMP-9 was utilized to explain the structure−activity relationship of our novel sulfonamide inhibitors. Molecular dynamics (MD) simulations of the complex models revealed important features of the binding mechanism of our inhibitors: (i) the ligand carboxylate group coordinating to the catalytic zinc ion and hydrogen bonding to the Glu219 side chain, (ii) one of the sulfonyl oxygens forming hydrogen bonds with the main chain NHs (Leu181 and Ala182), (iii) the sulfonyl substituent making extensive hydrophobic contact with the S1′ subsite. The gauche conformation exclusively adopted by the sulfonamide C−N−S−C torsion plays an important role in achieving the third binding feature by properly directing the substituent into the S1′ subsite. Improvement of the inhibitory activity according to straight elongation of the sulfonyl substituent was attributed to an increase of the hydrophobic contact between the substituent and the S1′ subsite. Structural modifications which alter the straight shape of the substituent lead to deterioration of the activity. On the other hand, the two candidate models selected for MMP-2 differ in the bottom shape of the S1′ subsite: one with a channel-like subsite and the other with a pocket-like subsite resembling that of the MMP-9 model. The bottom shape was experimentally probed by chemical synthesis of inhibitors having elongated sulfonyl substituents whose terminal alkyl groups were shown by MD simulations to protrude from the S1′ subsite bottom into the solvent. Gelatinase assays of these inhibitors showed that elongation of the substituent significantly reduces activity against MMP-9 while retaining activity against MMP-2, consequently increasing the selectivity between MMP-2 and -9. The results confirm that MMP-9 has a pocket-like S1′ subsite with a floorboard and MMP-2 has a channel-like S1′ subsite.

Introduction

Matrix metalloproteinases (MMPs) are zinc proteinases that cleave constituents of the extracellular matrix, which consists of a protein network of collagens, proteoglycans, and glycoproteins. The extracellular matrix functions as a medium of migration, attachment, and structural support in various cell types and tissues. Therefore, MMPs play a crucial role in matrix remodeling events of connective tissues during embryonic growth and wound healing.[1−4] MMPs can be categorized into several classes based on substrate specificity and domain structure: collagenases (MMP-1, -8, -13), which cleave triple-helical interstitial collagen; gelatinases (MMP-2, -9), which cleave denatured collagen, elastin, and type IV and V collagens; stromelysins (MMP-3, -10, -11), which mainly cleave proteoglycans; membrane-type MMPs (MMP-14, -15, -16, -17), which are associated with activation of pro-MMPs; and others (MMP-7, etc.). Among the subfamilies of MMPs, gelatinases have been considered very promising for use in drug development. Since gelatinases are thought to play an important role in triggering the processes of tumor growth, invasion, and metastasis by cleaving the vascular basement membrane which consists of type IV collagen, gelatinase inhibitors have been studied extensively in the search of a new type of anticancer drug.[5−9]

MMPs basically consist of a short signal peptide, a propeptide, a catalytic domain, a hinge region, and a hemopexin-like domain. Furthermore, gelatinases have a huge insertion called the fibronectin-like domain (FLD) in their catalytic domain (Figure 1). FLD is a series of three tandem domains that are homologous to the collagen-binding domain of fibronectin.[10] Considerable progress in determining three-dimensional structures of MMPs has been made by X-ray crystallography and NMR spectroscopy. Refined, high-resolution structures of MMP catalytic domain−inhibitor complexes have been obtained for MMP-1, -3, -7, and -8,[11−14] and the detailed structural information has enabled structure-based design of novel inhibitors. All the crystal structures available for these MMPs possess in common a core structure consisting of three α-helices and a five-

10.1021/jm980514x CCC: $18.00
Published on Web 04/24/1999

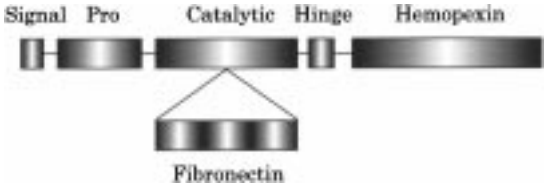

Figure 1. Schematic representation of the domain structure of gelatinases: signal, signal peptide; pro, propeptide domain that masks the active site in an inactive proenzyme form; catalytic, catalytic domain that contains a highly conserved catalytic zinc-binding site; hinge, hinge region; hemopexin, hemopexin-like domain that may be involved in matrix binding; fibronectin, fibronectin-like domain consisting of three tandem repeats that are homologous to the collagen-binding domain of fibronectin.

stranded β-sheet, a catalytic zinc ion located at the bottom of the catalytic cleft and coordinated by three histidine residues, other metal ions (zinc and calcium) which stabilize the catalytic domain core structure, and all catalytic residues.

Recently, we reported a series of novel sulfonamide inhibitors of gelatinases.[15] Although the molecular mechanism underlying their binding to the enzymes has not been clear due to lack of structural information of the gelatinase catalytic domains, the strong similarity among the structures of MMP-1, -3, -7, and -8 encouraged us to construct gelatinase models based on their crystal structures by using the homology modeling technique. In this study, we performed homology modeling of the gelatinase catalytic domains, tried to explain the structure−activity relationship developed in our previous study on the sulfonamide inhibitors using the gelatinase homology models, and then designed novel inhibitors based on the molecular mechanism we had established.

Results and Discussion

Homology Modeling of Gelatinases. Homology modeling[16−20] is a computational method widely used for building a protein model based on the known three-dimensional structure of the protein which has a moderate to high sequence similarity to that of the target protein. The accuracy of the protein models constructed by this method depends on the degree of amino acid sequence homology between the target and template proteins. In general, homology modeling with a sequence identity of less than 30% is quite challenging, while that with identity greater than 30% is expected to yield a model accurate enough to be used for subsequent modeling work. To analyze protein−ligand interaction or design novel compounds in a structure-based manner, a sequence identity of more than 50% may be required.

Multiple sequence alignment of the MMP catalytic domains showed a high sequence homology between gelatinases and the other MMPs with known three-dimensional structures, suggesting the striking similarity of secondary and tertiary structures within the MMP family (Figure 2). Indeed, as shown in Figure 3, all the crystal structures for MMP catalytic domains possess the same folding structure and are superimposable with pairwise root-mean-square (rms) deviations of 0.40−0.84 Å over the main chain atoms except for variable loops (residues 205−209, 241−247). Residues 241−247,

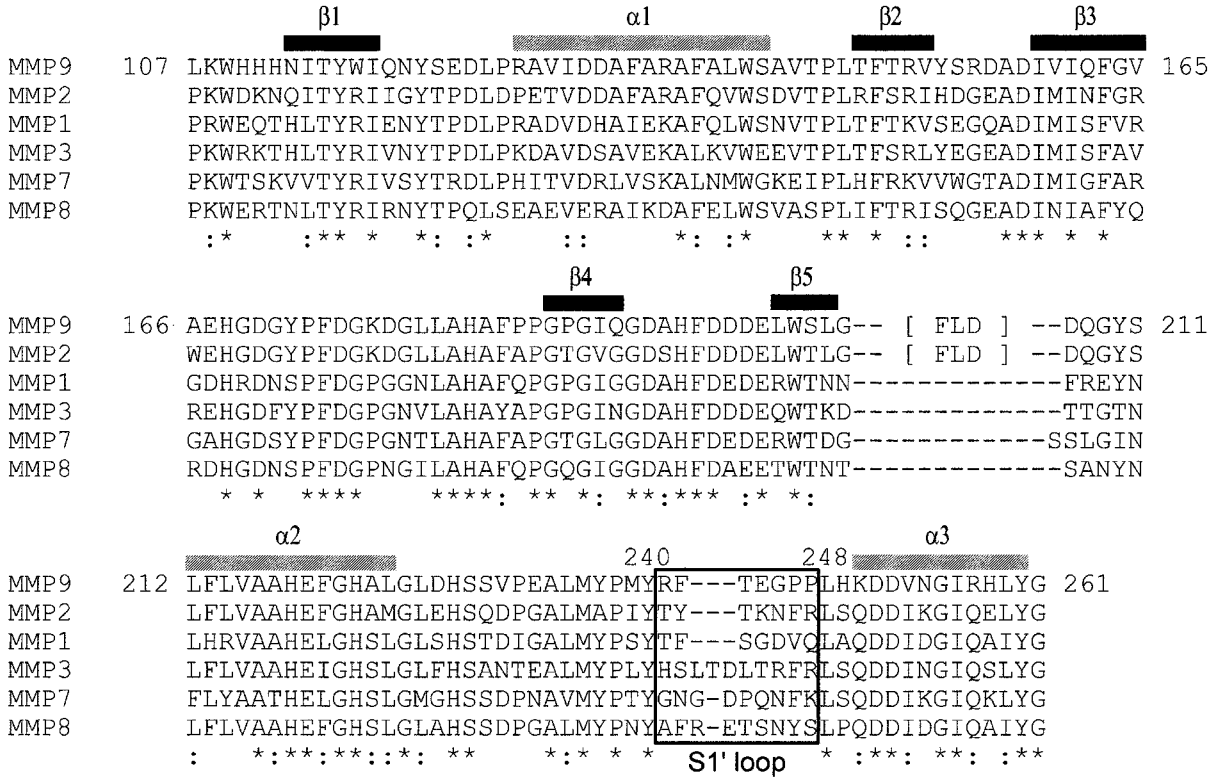

Figure 2. Multiple sequence alignment of the catalytic domains of gelatinases with those of the other MMPs with known three-dimensional structures. The secondary structure elements were taken from the crystal structure of MMP-1. The residue numbering is based on that of MMP-1. Gaps are indicated by hyphens. The S1′ loop region (residues 241−247) described in the text is surrounded by a rectangle: FLD, fibronectin-like domain; '*', identical residues in all six sequences; ':', similar residues by the definition of CLUSTAL X.

Figure 3. Tube-plot representation of the catalytic domains of MMP-1, -3, -7, and -8. The structures of MMP-3, -7, and -8 are superimposed onto that of MMP-1 by least-squares fit using the backbone atoms except for variable loops (residues 205−209 and the S1′ loop). The S1′ loops are indicated by cyan, yellow, green, and pink tubes for MMP-1, -3, -7, and -8, respectively. The figure was generated using MOLMOL.

which are color-coded in Figure 3 and surrounded by a rectangle in Figure 2, show conformational diversity within the MMP family. Since this segment forms the bottom half of the S1′ subsite, it is referred to hereafter as the "S1′ loop".

Comprehensive pairwise alignments of the catalytic domains for all pairs of the MMPs gave sequence identities ranging from 45% to 60%, where the FLD insertions in gelatinases were excluded from the alignments because the FLD was thought to be structurally independent of the rest of the catalytic domain. Among the MMPs with known three-dimensional structures, the MMP-3 catalytic domain showed the highest sequence identity with each member of the gelatinases, 57.0% with MMP-9 and 60.5% with MMP-2; hence the crystal structure of MMP-3 (Protein Data Bank entry: 1SLM) was selected as a template protein. These high sequence identities of MMP-3 led us to perform the subsequent homology modeling of the gelatinase catalytic domains.

Because the S1′ loop of MMP-3 is three residues longer than those of gelatinases and no particular sequence homology is observed between their S1′ loops (Figure 2), we searched for seven-residue fragments which could geometrically replace the S1′ loop segment of the MMP-3 template in a subset of the Brookhaven Protein Data Bank[21] and then checked for the conformational validity. This led us to choose the S1′ loop of MMP-1 as the most suitable seven-residue fragment. After the S1′ loop segment of the MMP-3 template was replaced with that of MMP-1, the template protein model was converted into gelatinase catalytic domain models by mutating the residues which were not identical between the resulting protein model and each gelatinase. The subsequent model refinement, however, gave improper conformations for the S1′ loop, in which the main chain torsion angles (ϕ, ψ) of some residues were located in the disallowed region of the Ramachandran plot, suggesting that the S1′ loop conformation of MMP-1 is unsuitable for accommodating the S1′ loop sequences of gelatinases. It is generally known that loop conformations are not always conserved even with the same loop length,[22] as we can see the conformational difference between the nine-residue S1′ loops of MMP-7 and -8, which are colored in green and pink, respectively, in Figure 3.

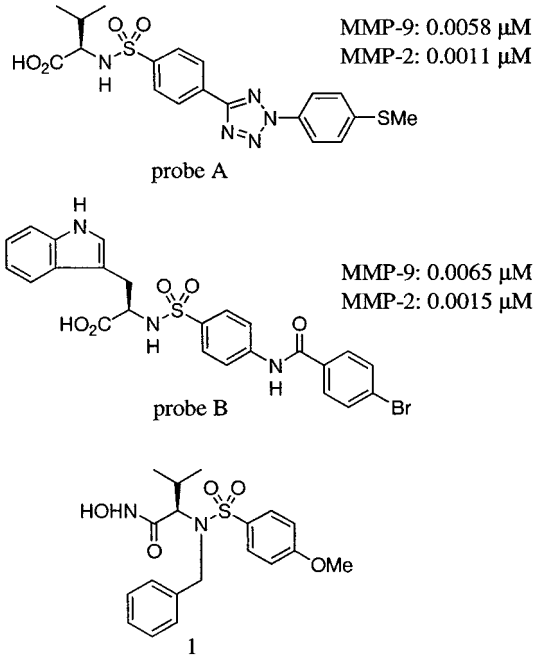

1

Figure 4. Chemical structures of two probe inhibitors used for the S1′ loop exploration and a Ciba-Geigy compound (**1**). Inhibitory activities (IC_{50}) of the probe inhibitors against MMP-9 and -2 are shown.

Exploration of the S1′ loop conformations was attempted using the simulated annealing method. Inspection and comparison of the series of crystal structures of the other MMPs revealed that the temperature factors of the S1′ loops are comparatively small and that the S1′ loop main chain retains its conformation upon inhibitor binding into the S1′ subsite. Therefore, the S1′ loop backbones of gelatinases were also expected to be rigid. To reasonably and effectively explore the conformational space, simulated annealing calculations were performed for the gelatinase models as complexes with "probe" inhibitors docked into the S1′ subsite. Exploration using a single probe inhibitor is likely to provide conformers biased to the probe used. If independent explorations using two or more different probe inhibitors provide similar conformers which are classified into a single group by some criteria, then such loop conformers could be considered as not biased to a particular probe and could be used in subsequent simulation study. Thus, we selected two equally potent inhibitors from our recently reported sulfonamide inhibitors:[15] probes A and B (Figure 4). Another characteristic considered in selecting reasonable conformers was the shape complementarity to the probe inhibitors. This was based on the assumption that the S1′ loops of gelatinases would have high shape complementarity to potent inhibitors bound to the S1′ subsite. Shape complementarity was evaluated using the buried surface area in the complex model, which is defined as the surface area desolvated upon inhibitor binding or complex formation.

The probe inhibitors were manually docked into the active site of the gelatinase models according to the binding mode observed in the crystal structure[23] of the MMP-1 complexed with Ciba-Geigy's inhibitor **1**, in such a manner that the negatively charged carboxylate group could be coordinated to the catalytic zinc ion, and the

Table 1. Exploration of the S1′ Loop Conformations of MMP-9

probe A			probe B		
model[a]	BSA[b]	cluster[c]	model[a]	BSA[b]	cluster[c]
A02	821	*a*	B19	831	*j*
A16	813	*b*	B02	820	*k*
A19	800	*b*	B12	816	*b*
A11	800	*c*	B11	816	*b*
A14	796	*d*	B09	808	*l*
A17	786	*e*	B17	807	*c*
A08	782	*f*	B20	804	*j*
A10	775	*f*	B18	800	*j*
A15	774	*d*	B14	800	*m*
A03	772	*g*	B06	798	*n*
A18	771	*e*	B16	792	*c*
A01	767	*h*	B07	785	*o*
A07	764	*d*	B08	780	*p*
A20	763	*i*			

[a] Model numbers sequentially given following the 20 cycles of simulated annealings for each probe inhibitor. [b] Buried surface area (BSA) between the probe inhibitor and the MMP-9 model in Å^2. [c] Cluster id for each model.

Table 2. Exploration of the S1′ Loop Conformations of MMP-2

probe A			probe B		
model[a]	BSA[b]	cluster[c]	model[a]	BSA[b]	cluster[c]
A01	807	*a*	B17	844	*i*
A11	800	*b*	B10	827	*j*
A19	798	*c*	B18	813	*i*
A17	798	*c*	B19	810	*k*
A10	794	*d*	B04	809	*l*
A18	790	*c*	B20	804	*i*
A03	790	*e*	B02	801	*m*
A12	786	*b*	B12	798	*n*
A16	784	*c*	B16	797	*o*
A20	778	*e*	B15	793	*p*
A06	778	*f*	B07	789	*q*
A14	778	*b*	B05	781	*r*
A13	775	*c*	B14	779	*s*
A02	761	*g*	B11	775	*r*
A07	761	*a*			
A15	745	*g*			
A08	736	*g*			
A09	719	*h*			

[a] Model numbers sequentially given following the 20 cycles of simulated annealings for each probe inhibitor. [b] Buried surface area (BSA) between the probe inhibitor and the MMP-2 model in Å^2. [c] Cluster id for each model.

sulfonyl substituent occupied the S1′ subsite. These initial docking models were then submitted to 20 cycles of simulated annealing protocol followed by energy minimization, giving 40 models for each gelatinase (20 models from each of the two probe inhibitors). These models were validated by examining the distributions of main chain (ϕ, ψ) and side chain (χ_1, χ_2) torsion angles of each residue on the S1′ loop using the PROCHECK program.[24] After eliminating the inappropriate models which had torsion angles in the disallowed region in the Ramachandran $\phi-\psi$ plot and/or the $\chi_1-\chi_2$ plots, we had a set of 27 models for MMP-9 and another set of 32 models for MMP-2.

To objectively classify these model sets according to the similarity of the S1′ loop conformation, each set was subjected to hierarchical clustering[25] in which rms deviations of main chain atoms in the S1′ loop were used as the dissimilarity measure between conformations. The clustering was done until the minimum intercluster distance exceeded the termination criterion of 1.5 Å. Table 1 gives the models for MMP-9 listed according to the probe used and in descending order of buried surface areas within each panel, together with the cluster id for each model. Table 2 presents this information for the set of MMP-2 models. From the 27 models of MMP-9, we obtained 16 clusters (*a*−*p*). Two clusters consist of models from both groups: cluster *b* (A16, A19, B11, and B12) and cluster *c* (A11, B16, and B17). The other clusters consist of only the models obtained with either probe A or B. Cluster *b* was selected because the buried surface areas of all models in it are significantly larger than those in cluster *c*. In cluster *b*, although the total buried surface area of A16 is slightly smaller than those of B11 and B12 as shown in Table 1, the buried surface area only at the interface between the S1′ subsite and the aromatic substituent attached to the sulfonyl group is significantly larger in A16 (640 Å^2) than in B11 (541 Å^2) and B12 (541 Å^2). Therefore, model A16 (MMP-9-A16) was chosen as the MMP-9 model (Figure 5). On the other hand, although the clustering of the 32 models of MMP-2 gave 19 clusters (*a*−*s*), all the clusters consisted of the models obtained with either probe A or B (Table 2). The hierarchical clustering was conducted further increasing the distance criterion, and the first cluster consisting of the models from both groups appeared at 2.6 Å, at which there were 11 clusters. The first shared cluster, however, contained pairs of models which were too dissimilar to each other to be assigned to a single cluster. Therefore, the model with the largest buried surface area was chosen as a representative of each group or panel in Table 2: A01 (MMP-2-A01) and B17 (MMP-2-B17). In this paper, model names such as MMP-9-A16 are used to denote unliganded protein models.

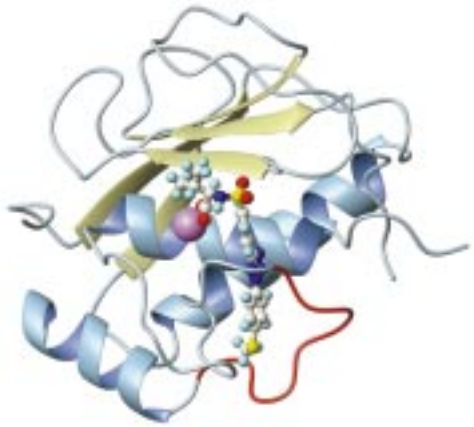

Figure 5. MMP-9-A16 model complexed with the probe A inhibitor. The protein model is represented by ribbon diagram, the probe molecule by ball-and-stick, and the catalytic zinc ion with a magenta sphere. The S1′ loop segment is indicated by red tube. The figure was generated using MOLMOL.

The three models were examined in terms of the numbers of exceptional residues, that is, the hydrophobic residues that are exposed to the solvent and the polar residues that are buried. Although there is no absolute criterion for the number of such residues by which a protein model is judged to be good or bad, one can expect that members of the same protein family should have comparable numbers of exceptional residues. The MMP-9-A16, MMP-2-A01, and MMP-2-B17 models contain 11, 7, and 7 exposed hydrophobic residues, respectively, while the numbers of such residues observed in the crystal structures of other MMPs are 5, 14, 10, and 7 for MMP-1, -3, -7, and -8, respec-

tively. The values for the three models are within the range (5−14) of those for the other MMPs. With respect to buried polar residues, the three models contain the same set of five residues, Asp170, Asp194, Asp198, Glu201, and Asp252, which are all conserved among the MMPs used in the multiple alignment (Figure 2) and consequently have not been substituted in the model building based on the MMP-3 template. In the three models, the first four residues interact with metal ions and the fifth residue forms hydrogen bonds to the main chain NH groups of Leu235 and Met236 as can be seen in the crystal structures of the other MMPs. Thus, these three models were qualified for subsequent model evaluation.

The structural validity of the three models was further evaluated by carrying out molecular dynamics (MD) simulations of each model complexed with its original probe inhibitor in the solvated system at room temperature. If the model contains geometrical strains, the simulation would induce appreciable conformational changes in the main chain structure to release the strains. Alternatively, if the model has valid geometries, then the simulation should show a steady state which does not deviate significantly from the crystal structures of the other MMPs. For each of the three models, the average structure, which was generated from 500 coordinate sets sampled during a 50-ps simulation, was compared with the MMP crystal structures, giving relatively small rms deviations of the backbone atoms except for the variable loops (residues 205−209, 241−247): 1.1−1.2 Å for MMP-9-A16, 0.9−1.1 Å for MMP-2-A01, and 0.9−1.1 Å for MMP-2-B17. Additionally, no significant conformational change was observed in the backbone of the S1′ loop during the simulation of each model. Thus, the validity of the three models was confirmed through the MD simulations, though no advantage or preference of one model over the other was indicated with respect to the two MMP-2 models. As will be discussed later, this issue was addressed by structure-based design of novel inhibitors.

Before discussing the SAR of our inhibitors in the following section, let us first note the residue composition of the catalytic site and S1′ subsite in the three models. The catalytic site residues which are in contact with the probe inhibitor A or B in the three models are residues 179−184, 219, 222, and 228. These nine residues are all conserved between MMP-2 and -9, forming essentially the same catalytic site surface among the models. The surface of the S1′ subsite is lined with several residues on the S1′ loop (residues 241−247) and 11 other residues (214, 215, 218, 232−235, 237−240). In addition to the remarkable sequence dissimilarity of the S1′ loop between the two gelatinases, the number and composition of the S1′ loop residues which form the inner surface of the subsite bottom half vary depending upon the loop conformations: six residues (241, 243−247) in MMP-9-A16, five residues (241−243, 246, 247) in MMP-2-A01, and five residues (241, 242, 244−246) in MMP-2-B17. On the other hand, 8 of the latter 11 residues are conserved (residues 214, 215, 218, 232, 234, 235, 238, 240), and the other 3 are mutated between MMP-2 (Gly233, Ala237, Ile239) and MMP-9 (Glu233, Tyr237, Met239). In the three gelatinase models, however, the nonconserved three residues

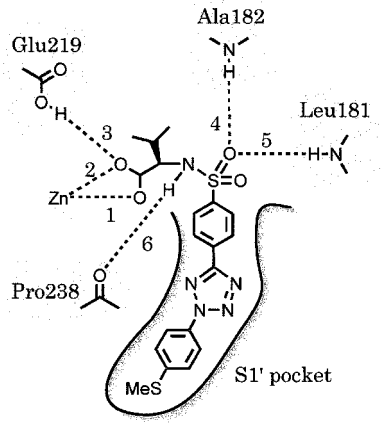

Interatomic Distance (Å)

1	[O ··· Zn]	2.0 ± 0.1
2	[O ··· Zn]	2.1 ± 0.1
3	[O ··· O]	2.8 ± 0.1
4	[O ··· N]	3.4 ± 0.3
5	[O ··· N]	2.9 ± 0.1
6	[N ··· O]	5.5 ± 0.4

Figure 6. Schematic representation of the polar interactions observed in the MD simulation of probe A bound to MMP-9-A16. The interatomic distances are given as mean values of those observed in 500 structures sampled during the MD simulation, accompanied by standard deviations.

project their side chains outward from the S1′ subsite, consequently forming nearly the same interior of the S1′ subsite.

Docking Simulation of Sulfonamide Inhibitors and Explanation of Structure−Activity Relationship. Binding features observed in the simulation of the probe A inhibitor docked into the MMP-9-A16 model are schematically represented in Figure 6 together with interatomic distances for all important polar interactions. Coordination of the inhibitor's carboxylate group to the catalytic zinc atom (bonds 1 and 2) was maintained for the entire simulation time, and one of the carboxylic oxygen atoms also formed a stable hydrogen bond to the Oϵ atom of Glu219 (bond 3), suggesting that the carboxylate group is the primary determinant, as in the case of other zinc-binding groups, such as a hydroxamate, for binding of our sulfonamide inhibitors. Two hydrogen bonds between one of the sulfonyl oxygens and the main chain nitrogens of Leu181 and Ala182 (bonds 4 and 5) were also shown to contribute to the complex stabilization, while the hydrogen bond to Ala182 (bond 4) was observed to be frequently cleaved in the simulation, giving an average distance longer than that for bond 5. Another hydrogen bond was observed between the sulfonamide nitrogen and the main chain carbonyl oxygen of Pro238 (bond 6) in the minimized starting structure of the MD simulation. Although the hydrogen bond was retained during the energy minimization stage of the initial complex model prepared by manual docking, the bond was cleaved because Pro238 moved away from the inhibitor during an equilibrium stage of the MD simulation. In the subsequent data sampling stage, no direct hydrogen bond between the sulfonamide nitrogen and the Pro238 carbonyl was observed, but a water-mediated hydrogen

Table 3. Effect of *N*-Methylation or Sulfonyl Replacement on Inhibitory Activities against MMP-9

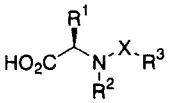

compd	R^1	R^2	X	R^3	IC_{50} (μM) [a]
2	$(CH_3)_2CH$-	H	$-SO_2-$	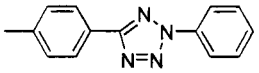	0.072
3	$(CH_3)_2CH$-	Me	$-SO_2-$		0.87
4	$PhCH_2$-	H	$-SO_2-$	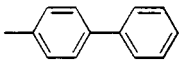	2.7
5	$PhCH_2$-	H	-CO-		> 20

[a] Concentration required for 50% inhibition of enzyme activity of MMP-9. Details of the enzyme assays are described in the Experimental Section.

bond was frequently found. The carbonyl oxygen of Pro238 is known to participate as a hydrogen bond acceptor in the binding of several peptidic inhibitors.[26,27] Babine and Bender[23] reported the movement of Pro238 in the MMP-1 crystal structure complexed with sulfonamide inhibitor **1**, which has a benzyl group on the sulfonamide nitrogen, with the explanation that the movement of Pro238 occurred in order to avoid collision with the "CH_2 group" of the *N*-benzyl substituent. In our case, however, even with the sulfonamide nitrogen being unsubstituted, the movement was observed in the MD simulation and found to be due to a collision between the benzene ring connected to the sulfonyl group and the flexible loop containing Pro238.

The SAR on novel sulfonamide inhibitors, which was developed mainly in our previous study[15] and also in this one, could be explained using MD simulations of representative inhibitors docked into the MMP-9-A16 model. First, potency reduction by N-alkylation of sulfonamide was accounted for using N-unsubstituted (**2**) and *N*-methyl (**3**) derivatives of D-valine sulfonamides (Table 3). In our preliminary docking study using crystal structures of the other MMPs as a rigid protein model, the potency reduction by the N-alkylation was ascribed to both the lack of a hydrogen bond expected with the N-unsubstituted derivative and the steric repulsion introduced by the *N*-alkyl group. In both simulations using **2** and **3**, Pro238 moved from its original position in a manner similar to the case of probe A, giving nearly identical mean values for the distance between the sulfonamide nitrogen and the carbonyl oxygen of Pro238: 5.3 ± 0.4 and 5.1 ± 0.4 Å for **2** and **3**, respectively, which are comparable to that observed in the simulation described above (Figure 6). The simulations indicated that compound **2** could form a water-mediated hydrogen bond to Pro238, but it did not persist due to frequent exchange of the bridging water molecule, and that the *N*-methyl group of **3** could fit into the space created by the Pro238 shift without inducing steric repulsion (Figure 7). Thus, small reduction of the potency caused by introducing a methyl group on the sulfonamide nitrogen was ascribed to the lack of the water-mediated hydrogen bond rather than steric repulsion.

Second, the replacement of the sulfonamide group of **4** with a carboxamide group led to quite a less potent inhibitor (**5**). This SAR was accounted for by significant change of overall shapes of the inhibitors which are determined by the conformation of the functional groups, sulfonamide in **4** and carboxamide in **5**, around its central bond. While it is widely known that carboxamide C−N−C(=O)−C torsion exclusively adopts the trans conformation if the amide nitrogen is not further substituted, the conformational profile of sulfonamide is not well-known. Thus far, docking of our sulfonamide inhibitors to the gelatinase catalytic domain models has been based on the gauche conformation observed[23] in the Ciba-Geigy inhibitor **1** bound to MMP-1. We analyzed the distribution of C−N−S−C torsion angles observed in crystal structures of both small molecules and protein−ligand complexes. Search of the Cambridge Structural Database[28] for small molecule crystal structures having C−N(H)−$S(O_2)$−C substructures retrieved 184 occurrences in 161 entries, providing a mean value of 68.8 ± 11.5° for absolute C−N−S−C torsion excluding two outliers larger than 120° (see Experimental Section for details). On the other hand, RELIBase[29] search of the Brookhaven Protein Data Bank[21] for protein−ligand complex crystal structures in which the ligand had a C−N(H)−$S(O_2)$−C moiety provided 16 complexes, which gave an absolute C−N−S−C torsion mean value of 71.1 ± 11.6° for 15 ligands excluding one outlier of 125.5°. The statistics of C−N−S−C torsion angles in crystal structures revealed that the torsion adopts an exclusively gauche conformation, ensuring us that the sulfonamide torsion is unlikely to adopt a trans conformation. Therefore, an MD simulation of **4** was performed with a docking mode similar to the cases of the other sulfonamide inhibitors (Figure 8a). The mean value of the absolute C−N−S−C torsion of **4** in this simulation was 70.4 ± 7.7°. On the other hand, manual docking of **5**, with the amide conformation fixed to trans, into MMP-9-A16 revealed that coordination of the carboxylate group to the zinc ion is possible only when the hydrophobic substituent is positioned in the shallow cleft consisting of S2′ and S3′ subsites but not in the S1′ subsite; hence an MD simulation was performed using the docking mode shown in Figure 8b. The two simulations showed a significant difference in the buried surface areas at the interface between the substituent and the protein (399 ± 13 $Å^2$ for **4** and 204 ± 70 $Å^2$ for **5**), suggesting that an interaction of the hydrophobic substituent with the S1′ subsite is much more extensive and consequently contributes much more to the stabilization of inhibitor binding than that with the S2′ and S3′ subsites (Figure 8c,d). Simulation of **5** also showed

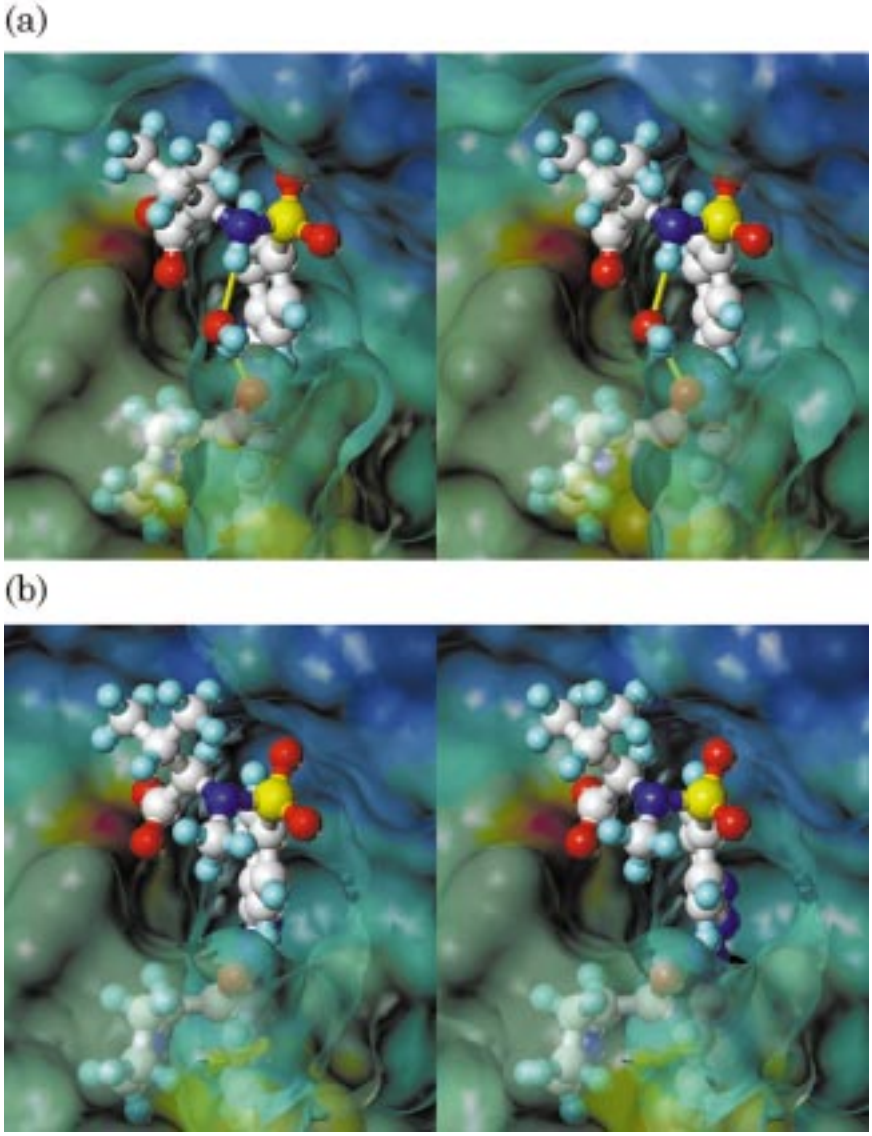

Figure 7. Stereoviews of the docking models of inhibitors **2** and **3** into MMP-9-A16. The figures are in the same orientation as in Figure 5. The inhibitor molecules and Pro238 are represented in ball-and-stick models. Electrostatic potential is mapped on the solvent-accessible surface of the protein. Part of the foreground surface which covers Pro238 and the sulfonyl substituent is shown translucently in order for these ball-and-stick models to be seen. (a) Docking model of inhibitor **2**. The sulfonamide nitrogen forms a water-mediated hydrogen bond to the carbonyl oxygen of Pro238. The bridging water molecule is shown in ball-and-stick, and the hydrogen bonds are indicated by yellow rods. (b) Docking model of inhibitor **3**. The methyl group on the sulfonamide nitrogen occupies the cavity where the bridging water molecule is located in panel a, without causing a serious steric repulsion. The electrostatic potential surfaces were generated with the MOLCAD module of SYBYL.

that the carboxamide moiety did not form any hydrogen bond to the enzyme. Thus, the sulfonamide group can play an important role in binding our inhibitors not only by forming hydrogen bonds to the enzyme but also by properly directing the hydrophobic substituent to the S1′ subsite and enabling it to plunge in deeply.

The D-phenylalanine series of compounds **4** and **6**−**8** show a clear tendency for a stepwise increase in MMP-2 and -9 inhibitory activities according to the straight elongation of the sulfonyl substituent, although the degree of activity increase against MMP-9 is more significant than that against MMP-2 (Table 4). Docking simulations of these inhibitors with the MMP-9-A16 model were performed, and the buried surface areas at the interface between the sulfonyl substituent and the S1′ subsite were calculated as a measure of hydrophobic interaction, with the expectation of a correlation between the activity and the buried surface area. As shown in Figure 9, the simulations demonstrated that replacement of the bromine atom of **6** with a phenyl (**4**), phenylacetylenyl (**7**), or biphenyl-4-yl (**8**) group increases the interface area. In particular, the straight hydrophobic substituent of **7** or **8** snugly occupies the long and narrow subsite and consequently makes extensive hydrophobic contacts with the subsite. These results are consistent with the increase of the buried surface areas from 314 ± 12 Å^2 (**6**) to 399 ± 13 Å^2 (**4**), 484 ± 16 Å^2 (**7**), and 577 ± 18 Å^2 (**8**). Thus, the length of the sulfonyl substituent is the critical attribute for potent inhibitors.

From the viewpoint of the fit, the shape of the substituent is also important for hydrophobic interaction. As shown with the compounds listed in the lower panel of Table 4, structural changes which alter the straight shape of the sulfonyl substituent lead to significant changes in inhibitory activities. Introduction of a nitro group (**9** vs **10**) and transposition of the

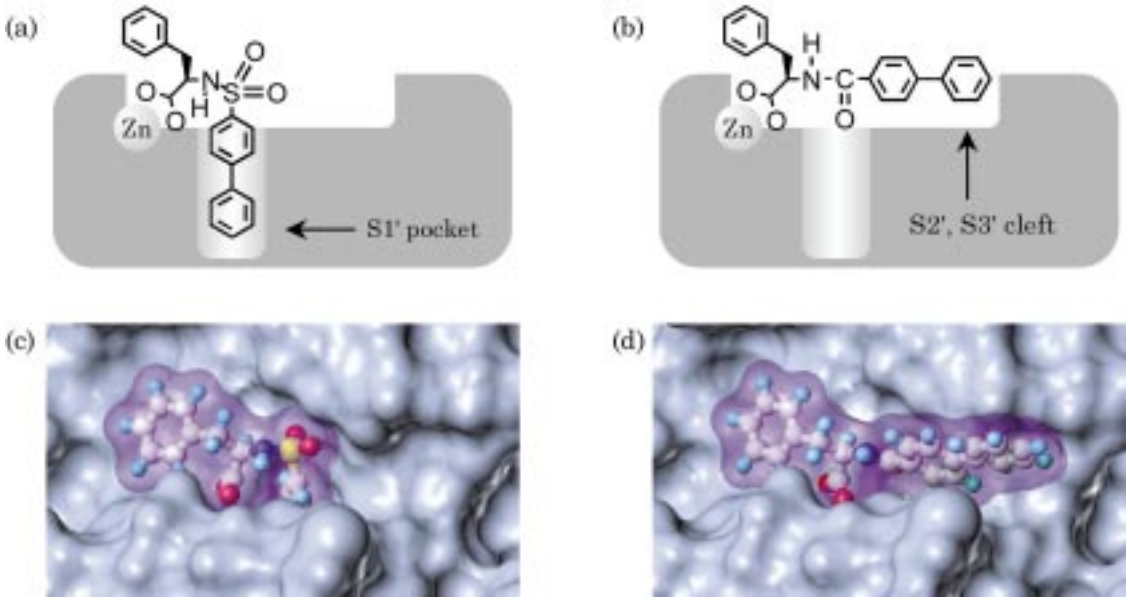

Figure 8. Docking models of inhibitors **4** and **5** into MMP-9-A16. (a,b) Schematic drawings of the side view of the docking models. (c,d) Surface representations viewed from the orientation in panels a and b rotated approximately 45° around the horizontal axis, showing the binding cleft to the viewer. The inhibitor molecules are each presented in ball-and-stick model within its translucent solvent-accessible surface. (a,c) Docking model of sulfonamide inhibitor **4**. The C−N−S−C torsion adopts a gauche conformation, enabling the biphenyl substituent to plunge in the S1′ subsite deeply. (b,d) Docking model of carboxamide inhibitor **5**. The C−N−C(=O)−C torsion adopts a trans conformation, directing the biphenyl substituent to the shallow S2′ and S3′ subsites.

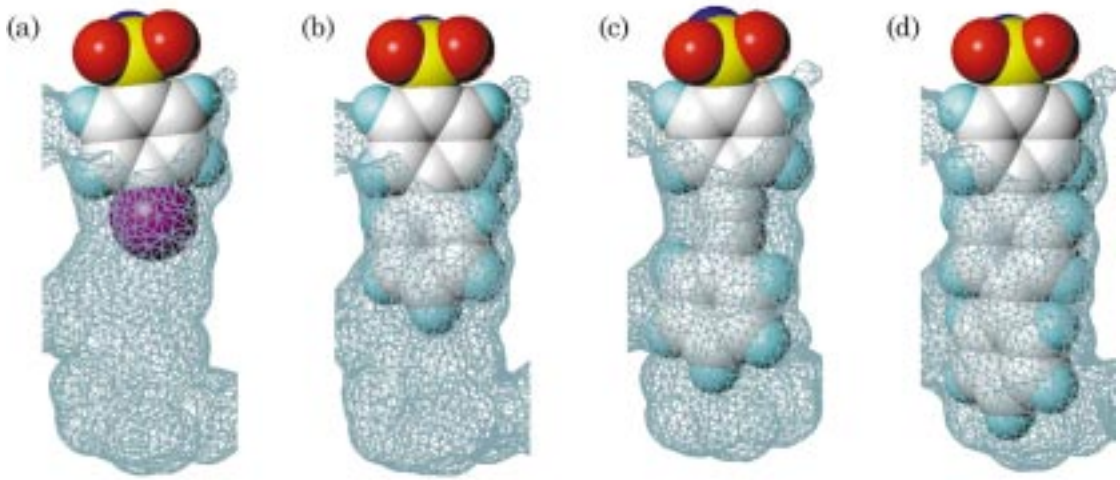

Figure 9. Space-filling models of the sulfonyl substituents of compounds **4** and **6**−**8** interacting with the S1′ subsite of MMP-9-A16. The inner surfaces of the S1′ subsite are represented with a triangle mesh. The models are viewed from the right of Figure 5. (a−d) Compounds **6**, **4**, **7**, and **8** are shown, respectively.

terminal methyl group from the para- to the ortho-position on the benzene ring (**11** vs **12**) significantly reduce the activities. The sulfonyl substituent of compound **9** is assumed to tightly fit the subsite in a manner similar to that of **7** as shown in Figure 9c, with no space left for substitution on the benzene rings. Therefore, significant reduction of activities observed for **10** against **9** can be attributed to a steric repulsion between the *o*-nitro group of **10** and the wall of the subsite. A similar degree of potency reduction of **12** against **11** can also be explained by the same steric reason as that described for **10**. Moderate activities retained for **10** and **12** suggest that the S1′ subsite can accommodate the substituents with a small lateral protrusion such as a nitro or methyl group if the rest of the substituent is in sufficient hydrophobic contact with the subsite to compensate for the steric repulsion caused by the protrusion. The reduction of activities from **9** to **10** and from **11** to **12** is smaller in the MMP-2 assay (ca. 50-fold) than in the MMP-9 assay (ca. 200-fold). This result suggests that the S1′ subsite of MMP-2 shows greater tolerance to the structural changes in the R^2 substituent than that of MMP-9.

The nearly equipotent inhibitors **9** and **11** differ in the linearity of the arylsulfonyl moiety (SO_2-R^2), that is, the angle between the two bond vectors extending from the aromatic ring attached to the sulfonyl group. Compound **11** has an angle of approximately 152° due to its 2,5-disubstituted thiophene ring, while the corresponding para-disubstituted benzene ring of **9** offers an angle of 180°. To examine how the angle difference is accommodated without affecting the binding affinity,

Table 4. Effect of the Length and Shape of Sulfonyl Substituents on Inhibitory Activities against MMP-9 and MMP-2

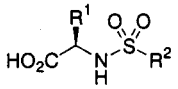

compd	R^1	R^2	IC_{50} (μM)[a]	
			MMP-9	MMP-2
6	$PhCH_2$-	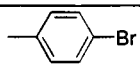	> 20	7.1
4		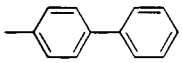	2.7	0.065
7		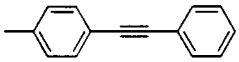	0.34	0.020
8		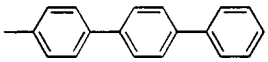	0.012	0.0044
9		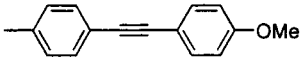	0.0082	0.00065
10		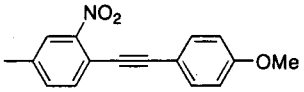	1.9	0.033
11		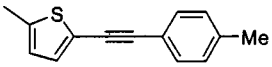	0.0096	0.0017
12	(3-indolyl)CH_2-	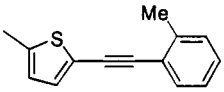	1.7	0.081
13		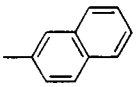	> 20	0.50
14		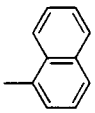	> 20	> 20

[a] Concentration required for 50% inhibition of enzyme activity. Details of the enzyme assays are described in the Experimental Section.

docking simulations of **9** and **11** in the MMP-9-A16 model were performed, and then average structures of the complex models were superimposed using main chain atoms of all residues in the protein. The superposition showed that the arylsulfonyl groups of the ligands are aligned so that the sulfonyl oxygen which is hydrogen-bonded to the protein remains in the same position and the line segments from the sulfonyl sulfur to the centroid of the terminal benzene ring overlap each other, tilting the sulfonyl substituent of **11** from that of **9** by 8°. Although the centroid of the thiophene ring of **11** is thus shifted aside slightly (ca. 0.5 Å) from that of the corresponding benzene ring of **9**, the R^2 substituent of **11** occupies the narrow S1′ pocket without causing severe steric overlap of the 3,4-positions of the thiophene ring with the wall of the pocket.[30] The *N*-sulfonylamino acid parts of the ligands overlap well at the carboxyl group and one of the sulfonyl oxygens, but show deviation at the sulfonyl sulfur, the sulfonamide nitrogen, and the amino acid α-carbon. Statistical analysis of the five interatomic distances corresponding to the bonds 1−5 in Figure 6 and the two torsion angles C−S−N−C and S−N−C−C(OOH) which were observed in the two simulations indicated that the common parts of the inhibitors **9** and **11** maintain all the important polar interactions (bonds 1−5) outside the S1′ pocket similarly to those shown in Figure 6 by altering the C−S−N−C and S−N−C−C(OOH) torsions. Thus, the angle difference (180° vs 152°) between **9** and **11** is accommodated by altering the conformation of the *N*-sulfonylamino acid part and by tilting the sulfonyl substituent, without significantly affecting either the polar interactions in the catalytic site or the hydrophobic interaction in the S1′ subsite.

The linearities of the naphthylsulfonyl groups in compounds **13** and **14**, which are defined as the angle between the bond vector from the aromatic ring to the sulfonyl sulfur and the vector connecting the two centroids of benzene rings in the naphthyl group, are estimated to be 150° for β-naphthyl of **13** and 90° for α-naphthyl of **14**. Taking into account the simulation results of compounds **9** and **11** described above, the β-naphthyl group of **13**, which has an angle value similar to that of **11**, is thought to occupy the S1′ subsite. However, it is unlikely that the group can make extensive hydrophobic contact with the subsite, because the β-naphthyl group is much smaller than the sulfonyl substituent of **11** and comparable to something between those of compounds **6** and **4**. Therefore, the weak activities of **13** relative to those of **9** or **11** can be attributed to the small size of its naphthyl group rather than to the bent shape (150°) of the β-naphthylsulfonyl group. The very weak activity of **14** even against MMP-2 indicates that the α-naphthyl group of **14** is hindered from occupying or interacting with the S1′ subsite due to its right-angled shape. Thus, it might be reasonable

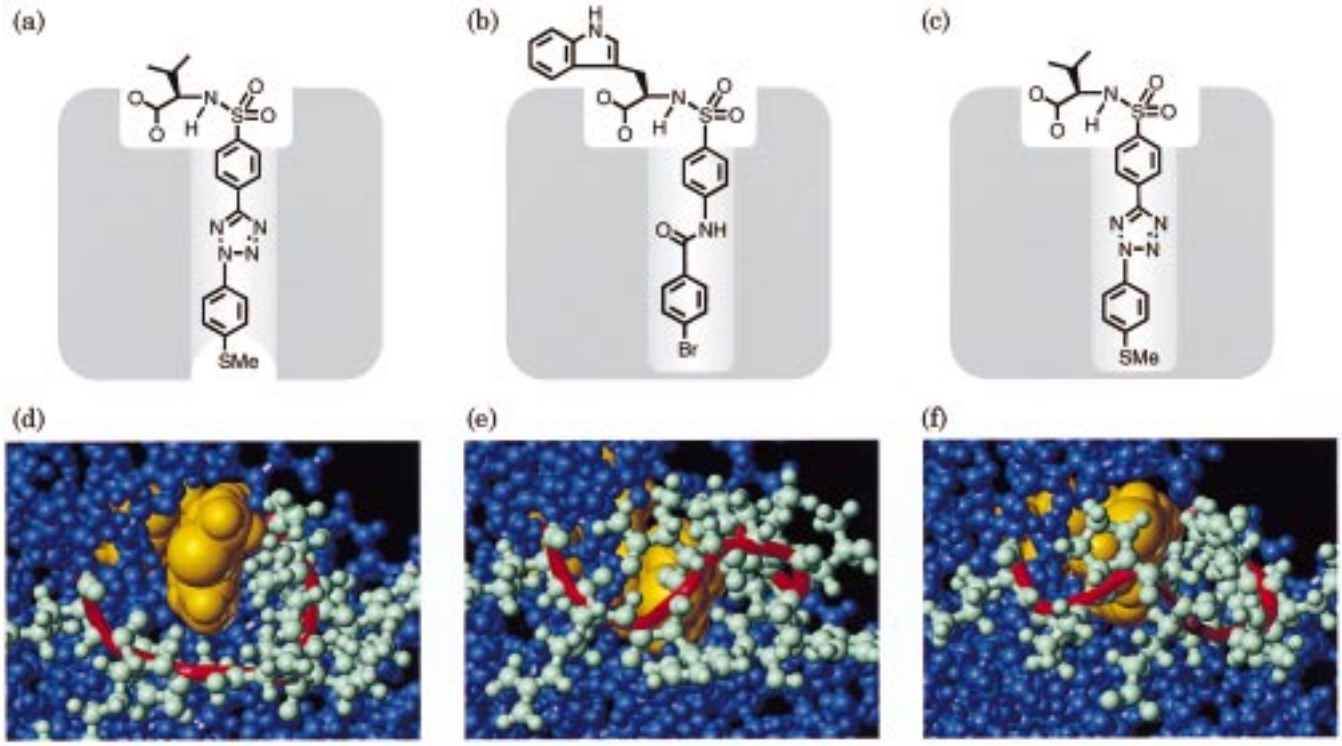

Figure 10. Comparison of the bottom shape of the S1′ subsites. (a−c) Schematic drawings of the side view of the S1′ subsites occupied by the probe inhibitors. (d−e) Ball-and-stick representations of the gelatinase models viewed from the bottom side of the S1′ subsite. The S1′ loop residues are colored in light green and the rest of the protein in purple, with Cα tracing of the S1′ loop represented as a red tube. The probe inhibitors are shown as a space-filling model colored in yellow. (a,d) MMP-2-A01 complexed with probe A. The S1′ loop does not block the bottom mouth of the S1′ subsite; hence the terminal methylthio group is exposed to solvent. (b,e) MMP-2-B17 complexed with probe B. The S1′ loop traverses the bottom mouth, forming a floorboard. (c,f) MMP-9-A16 complexed with probe A. The bottom shape is similar to that of MMP-2-B17.

to conclude that the sulfonyl substituent is one of the important factors influencing the binding affinity of our sulfonamide inhibitors and that an unbranched straight substituent of proper length is indispensable for attaining high inhibitory activities.

Probing the S1′ Subsite Bottom Shape of Gelatinases Using Novel Inhibitors with Elongated Hydrophobic Substituents. By homology modeling of the gelatinase catalytic domain, two models (MMP-2-A01 and MMP-2-B17) were obtained for MMP-2, while a single model (MMP-9-A16) was selected for MMP-9. The two MMP-2 models differ in the conformation of the S1′ loop, which forms the bottom half of the S1′ subsite. In MMP-2-A01, the S1′ subsite has no floorboard, forming a long and narrow "channel" with the bottom mouth not blocked by the S1′ loop. The complex model with probe inhibitor A shows that the terminal methylthio group of the probe molecule is exposed to solvent at the bottom end of the channel (Figure 10d). On the other hand, the S1′ loop of MMP-2-B17 traverses the bottom end opening of the channel and consequently forms the floor of the S1′ pocket (Figure 10e). Despite the difference in the bottom shape of the S1′ pocket, the model evaluations we previously performed on the two MMP-2 models showed no apparent advantage of one model over the other (vide supra). The MMP-9-A16 model (Figure 10f) has a S1′ pocket shape similar to that of MMP-2-B17.

To verify the MMP-9-A16 model and to determine the final model for MMP-2, we tried to experimentally probe the bottom shape of the S1′ subsite by synthesizing some inhibitors having an elongated hydrophobic substituent and then measuring their inhibitory potency against MMP-9 and -2. For this, novel inhibitors (**15**−**18** and **20**−**23**) were designed based on two parent inhibitors (**11** and **19**) by replacing the para-substituents (R^2 = Me) of the terminal benzene ring with longer hydrophobic groups (Et, *n*-Bu, O-*n*-Bu, and OPh) (Table 5). If the S1′ subsite has a channel-like shape such as that seen in the MMP-2-A01 model, the longer hydrophobic substituents of the designed inhibitors could be docked into the S1′ subsite, allowing the para-substituent to protrude from the bottom mouth of the channel. Docking simulation between **17** and MMP-2-A01 has demonstrated that the terminal methyl group of the butoxy substituent would protrude from the subsite channel, without causing significant steric repulsion (Figure 11). Therefore, the designed inhibitors are expected to have a potency comparable to those of their parent compounds. On the other hand, if the S1′ subsite has a floorboard similar to that of MMP-9-A16 or MMP-2-B17, and if the para-substituent is large or long enough to make severe steric overlaps with the floorboard, then the inhibitory potency of the designed inhibitors would significantly decrease due to the steric clash between the para-substituents and the floorboard.

The upper panel of Table 5 shows the gelatinase inhibitory activities of the D-tryptophan series of compounds (**11**, **15**−**18**). Elongation of the para-substituent from Me (**11**) to Et (**15**) did not affect the activities against both gelatinases. Further elongation of the substituent (**16**−**18**) resulted in striking reduction of activities (1/274−1/370) in the MMP-9 assay, but only slight decrease against MMP-2. Consequently, selectiv-

Table 5. Effect of Elongated Hydrophobic Substituent on Inhibitory Activities against MMP-9 and MMP-2

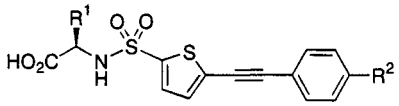

compd	R^1	R^2	IC_{50} (μM) [a] MMP-9		MMP-2		selectivity [c]
11		-Me	0.0096	(1) [b]	0.0017	(1) [b]	6
15		-Et	0.0073	(1)	0.0015	(1)	5
16	(3-indolyl)CH_2-	-nBu	2.7	(1/370)	0.0044	(1/3)	614
17		-O-nBu	2.0	(1/274)	0.0039	(1/3)	513
18		-OPh	2.3	(1/315)	0.010	(1/7)	230
19		-Me	0.024	(1/5)	0.0059	(1)	4
20		-Et	0.0044	(1)	0.0048	(1)	1
21	$(CH_3)_2CH$-	-nBu	0.21	(1/48)	0.0054	(1)	39
22		-O-nBu	0.21	(1/48)	0.0047	(1)	47
23		-OPh	0.26	(1/59)	0.018	(1/4)	14

[a] Concentration required for 50% inhibition of enzyme activity. Details of the enzyme assays are described in the Experimental Section. [b] Ratios of inhibitory activities to those of the most active compound (**15** or **20**). [c] Selectivities against MMP-2 over MMP-9 are expressed as the ratios of IC_{50} values for MMP-9 to those for MMP-2.

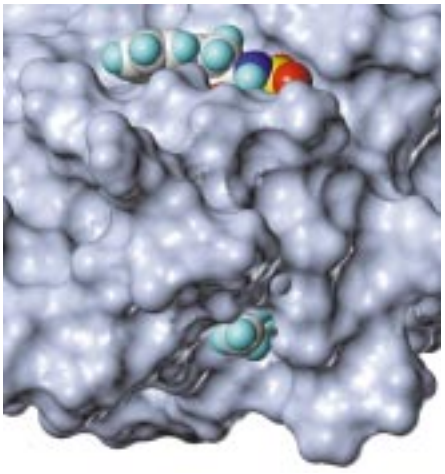

Figure 11. Docking simulation of inhibitor **17** into MMP-2-A01. The protein is represented with solvent-accessible surface and the inhibitor molecule with a space-filling model. The terminal methyl group of the inhibitor protrudes from the S1′ subsite channel.

ity against MMP-2 over MMP-9 was increased by approximately 40−100 times from that of the parent compound **11**. In the D-valine series of compounds (**19**−**23**) (the lower panel of Table 5), the ethyl derivative **20** is 5 times more potent in the MMP-9 assay than its parent compound **19**, and the compounds with a longer para-substituent (**21**−**23**) show significant reduction (1/48−1/59) of MMP-9 inhibitory activities relative to the most active compound **20**. On the other hand, the activities against MMP-2 are conserved for these inhibitors. Thus, irrespective of the α-substituent R^1 of the amino acid part, significant reduction of inhibitory activities was observed for MMP-9, but not for MMP-2. These results support a pocket-like S1′ subsite with a floorboard for MMP-9 and a channel-like S1′ subsite for MMP-2. This SAR may be alternatively explained by a deeper S1′ pocket in MMP-2 than in MMP-9, which can accommodate the large para-substituents. However, since the length of the S1′ loop in MMP-2 is the same as that in MMP-9 and is limited to seven residues, it is unlikely that MMP-2 has a deeper S1′ pocket than MMP-9. Furthermore, in contrast with the SAR shown in the upper panel of Table 4, the MMP-2 inhibitory activities of the compounds in Table 5 are insensitive to the length of the para-substituent, suggesting that the methyl (**11**, **19**) or ethyl (**15**, **20**) derivatives have already reached their maximal activities against MMP-2 and that further elongation of the para-substituent leads to no additional hydrophobic contact with the S1′ subsite. Therefore, a "channel-like" shape can be reasonably proposed for the S1′ subsite of MMP-2. These experimental results confirm the validity of the MMP-9-A16 model and lead us to select MMP-2-A01 as an appropriate MMP-2 catalytic domain model, consequently indicating that the S1′ subsite should be critical for increasing the MMP-2 vs MMP-9 selectivity among the gelatinases.

Finally, when compared with each pair of compounds having an identical para-substituent (R^2 = *n*-Bu, O-*n*-Bu, or OPh) from the two series of compounds (**16** vs **21**, **17** vs **22**, **18** vs **23**), the MMP-9 inhibitory activity of the compound from the D-valine series is 1 order of magnitude more potent than that of the corresponding compound from the D-tryptophan series. Although the activity difference is significant, a rational explanation for the effect of the R^1 substituent on this difference is difficult to offer and must await the determination of the three-dimensional structures of the MMP-9 complexes with these inhibitors.

Conclusions

We have constructed homology models for the catalytic domains of gelatinases based on the X-ray crystal structure of MMP-3, neglecting the FLD insertions in the gelatinase catalytic domains. The multiple sequence alignment and the superposition of the MMP crystal structures revealed that the main chain overall conformations of catalytic domains are well-conserved among the MMP family while conformational diversity is localized at the S1′ loop segment, which forms the bottom half of the S1′ subsite. Conformational exploration of the gelatinase S1′ loop was performed by simulated annealing of the complex model with the two highly potent "probe" inhibitors docked into the S1′ subsite. The explored conformations were classified by applying the hierarchical clustering method, and their shape complementarity to the probe ligand was estimated from the buried surface area within the complex model; then the representative model was selected for each gelatinase. The clustering results showed that the conformational space of MMP-9 explored with probe A overlaps with that explored with probe B, allowing us to select the reasonable representative model for MMP-9 (MMP-9-A16), while the simulated annealing for MMP-2 explored two separate spaces which are biased to each probe and have no overlapping region, giving two representative models: MMP-2-A01 and MMP-2-B17. The average structures of the models in the MD simulations showed relatively small rms deviations of main chain atoms ranging from 0.87 to 1.22 Å against the crystal coordinates of the other MMPs.

The SAR developed within our novel sulfonamide inhibitors was explained by performing MD simulations of the MMP-9-A16 model complexed with the inhibitors. Important features for the binding mechanism of our inhibitors have emerged: (i) coordination and hydrogen bond of the ligand carboxylate group to the catalytic zinc ion and the Glu219 side chain, (ii) hydrogen bonds of one of the sulfonyl oxygens to the main chain NHs (Leu181 and Ala182), (iii) extensive hydrophobic contact between the sulfonyl substituent and the S1′ subsite. Search of crystal structure databases revealed that the sulfonamide C−N−S−C torsion exclusively adopts a gauche conformation, by which the sulfonyl substituent is properly directed to the S1′ subsite, achieving the third binding feature. Hydrophobic interaction at the S1′ subsite is responsible for the SAR in that the straight elongation of the sulfonyl substituent improves inhibitory activity, while alteration of the straight shape of the substituent leads to deterioration of the activity. Thus, the sulfonamide moiety and its hydrophobic substituent play a critical role in the binding of our inhibitors. The two MMP-2 models differ in the bottom shape of the S1′ subsite: MMP-2-A01 has a channel-like subsite, and MMP-2-B17 has a pocket-like subsite resembling that of MMP-9-A16. The bottom shape was experimentally probed by chemical synthesis of the inhibitors having elongated sulfonyl substituents which were designed to protrude from the bottom of the S1′ subsite. Elongation of the sulfonyl substituents significantly reduced activities against MMP-9 while retaining activities against MMP-2 and consequently increased the selectivity between MMP-2 and -9. The assay results confirmed that MMP-9 has a pocket-like S1′ subsite with a floorboard and MMP-2 has a channel-like S1′ subsite, suggesting MMP-2-A01 to be more appropriate as an MMP-2 model than MMP-2-B17. Although reasonable protein models for the gelatinase catalytic domain have been constructed and the SARs of our sulfonamide inhibitors have been successfully explained by docking simulations using the homology models, high-resolution crystal structures of gelatinase catalytic domain−inhibitor complexes need to be solved to verify the accuracy of the models and to design novel inhibitors with improved selectivity between MMP-2 and -9.

Experimental Section

Molecular modeling and other graphical manipulations were performed using the SYBYL 6.4 software package.[31] Energy minimizations and MD calculations were done with the AMBER 4.1 program,[32] using the all-atom model force field. All inhibitor molecules used in this study were modeled using SYBYL and the Tripos force field, and their atomic charges were calculated with the semiempirical MNDO method implemented in the MOPAC program.[33] Schematic representations of the models were prepared with the MOLMOL program[34] and SYBYL.

Sequence Alignment and Selection of Template Protein. Amino acid sequences of the MMPs used in this study were obtained from GenBank.[35] Multiple and pairwise sequence alignments were performed with respect to the catalytic domain residues using the CLUSTAL X program[36] with default parameters. To maximize sequence identity in the alignment, the FLD insertions were removed from the sequences of gelatinases. For simplicity of residue numbering of MMPs, which was otherwise complicated by insertions and deletions between family members, the residue numbering of MMP-1 was applied to the aligned multiple sequences in Figure 2 so that all the residues important for substrate binding or structure holding could have the same numbers among the MMPs. Since the pairwise sequence alignments showed that the MMP-3 catalytic domain had the highest sequence identity with each gelatinase: 57.0% with MMP-9 and 60.5% with MMP-2, the crystal structure of MMP-3 was selected as a template protein.

Model Building. The atomic coordinates of crystal structure of MMP-3 were retrieved from the Brookhaven Protein Data Bank[21] (entry: 1SLM). Next, water molecules, the propeptide segment (Leu16−Ile89 in the 1SLM numbering), and three C-terminal proline residues were removed from this coordinate set, giving a template catalytic domain model. Seven-residue fragments which could replace the 10-residue S1′ loop (His224−Arg233 in the 1SLM numbering) of the template model were retrieved from the protein database, which is a subset of the Brookhaven Protein Data Bank,[21] using the Loop Search command of SYBYL with the default geometrical criteria. The retrieved fragments were further evaluated for their validity with respect to conformational similarity with the S1′ loop of the other MMPs and sequence similarity with the S1′ loop of the gelatinases, resulting in the S1′ loop of MMP-1 as the most suitable fragment. After the S1′ loop fragment of the template was replaced with that of MMP-1, all the side chains except for the conserved residues were mutated to those of the target gelatinase using the MUTATE command of SYBYL (67 residues for MMP-9 and 59 residues for MMP-2). Hydrogen atoms were added with standard geometry. Finally, to simulate the insertion point of FLD, the main chain was cleaved at the peptide bond between Gly206 and Leu207, and the termini were modified as a methyl amide for Gly206 and an acetamide for Leu207.

Model Refinement. The force-field parameters for two zinc atoms and their peripheral residues were determined according to Merz et al.[37] As the first step of refinement, all close contacts caused by the mutation of side chains were fixed by manually rotating the χ_2 torsion first, then χ_1 only if necessary, keeping the side chain torsions of the conserved residues in

their original conformation. Next, water molecules were added within a sphere of 28 Å radius from the center of the model. The model was refined according to the following protocol: (i) relaxation of all hydrogen atoms with all heavy atoms frozen using the BELLY option, (ii) 10-ps MD simulation of the water molecules at room temperature with an integration time of 2 fs applying the CAP and all-bonds SHAKE options, (iii) relaxation of the resulting system using a harmonic force constraint of 10.0 kcal/mol·Å^2 on all the backbone atoms, (iv) relaxation of the whole system without any constraint. In the above protocol, a nonbond cutoff of 10.0 Å and a constant dielectric of 1.0 were used, and 100 cycles of steepest-descent followed by 1900 cycles of conjugate-gradient minimization were applied to the relaxation stages.

Exploration of the Conformational Space of the S1′ Loop Using Simulated Annealing. After the probe inhibitor was manually docked into the gelatinase model as described in the text, the conformational space of the nine-residue segment consisting of the S1′ loop and its adjoining residues (Tyr240−Leu248) was searched using a combination of high-temperature MD calculation and energy minimization. During the simulation, the S1′ loop residues (Arg241−Pro247 in MMP-9 and Thr241−Arg247 in MMP-2) were allowed to move freely, and the two adjoining residues (Tyr240 and Leu248) were tethered with harmonic force constraint, while the rest of the system was frozen. To effectively explore the conformational space, solvent molecules were not included in the system. Since some preliminary simulations using 1*r* distance-dependent dielectric constant demonstrated that the loop conformation was prone to be stalled in a local well of the potential energy surface presumably due to strong electrostatic interaction, an increased dielectric constant (4*r*) was used during high-temperature simulation. That is, simple simulated annealing was performed in vacuo according to the following procedure: (i) 10 ps of simulation at 900 K using a dielectric constant of 4*r*, (ii) 4 ps of simulation at 300 K using a dielectric constant of 1*r*, (iii) 1000 cycles of minimization, with the resulting model being saved and then used as the initial structure for the next cycle of simulation. This procedure was repeated 20 times for each of the four complexes between the two gelatinase models and the two probe inhibitors, and the resulting 20 models were each refined in a solvated system according to the protocol described in Model Refinement.

Hierarchical Clustering of Gelatinase Model Sets. Clustering of each set of gelatinase models was carried out in two steps: (i) calculation of interconformational distances for all pairs of models and (ii) hierarchical clustering of the models based on the set of distances calculated in step (i). For each set, rms deviations of the main chain atoms on the S1′ loop were calculated for all pairs of models as interconformational distances using a SYBYL macro program created for this purpose, obtaining 351 distances from 27 MMP-9 models and 496 distances from 32 MMP-2 models. Usually, hierarchical clustering starts with singleton clusters and proceeds by merging together two clusters which give the minimum intercluster distance and subsequently recalculating intercluster distances; therefore the number of clusters decreases one by one, and the minimum intercluster distance increases according to the progress of the clustering. The clustering then terminates when the number of clusters becomes equal to a user-specified number or the minimum intercluster distance exceeds a user-specified distance criterion. Clustering of the two sets of gelatinase models was carried out using our original program written with the Perl language. This program reads a set of distances and performs cluster merging using one of the several clustering methods implemented in the program. Among the several clustering methods[25] with different definitions of the intercluster distance, the complete link method (or the farthest neighbor method) was applied to the above clustering tasks. In this method, the distance between two clusters is defined as that between the most distant pair of elements, one in each cluster. After preliminary clustering trials, the distance criterion was set equal to 1.5 Å; then hierarchical clustering of the two sets was performed. As a result, the 27 MMP-9 models were grouped into 16 clusters and the 32 MMP-2 models into 19 clusters.

Buried Surface Area Calculation. Buried surface areas at protein−ligand interface were calculated using Connolly's MS program,[38] which was invoked from within our original pre/postprocessing program written with the Perl language. Surface point calculation by the MS program[38] was carried out on the selected set of atoms around protein−ligand interface, neglecting water molecules. The probe radius was set equal to 1.5 Å, and van der Waals radii were taken from the ATOM_DEF atomic parameter file in SYBYL. The buried surface areas listed in Tables 1 and 2 were calculated with respect to only the protein and ligand atoms located inside the box which was 8 Å larger in all directions than that circumscribed around the ligand molecule. In the calculations of the buried surface areas at the interface between the sulfonyl substituent and the protein in the complexes of the compounds **4**−**8**, only the hydrophobic substituent attached to the sulfonyl group was used as the ligand part to consider, neglecting the rest of the ligand molecule, and then the protein atoms were selected as above. Given a single coordinate set file or a trajectory file generated from an MD simulation, the pre/postprocessing program reads in each coordinate set, determines the set of atoms for which surface points are calculated, invokes the MS program, sums up small patches of buried surface points separately for each atom, and finally generates the total buried surface areas.

Molecular Dynamics Simulation at Room Temperature. All the MD simulations at room temperature were performed with water molecules added within a sphere of 28 Å radius from the center of each model and using the following conditions: nonbond cutoff of 10.0 Å, dielectric constant of 1.0, integration time of 2 fs, and SHAKE option for all bonds. Each simulation was carried out according to the following protocol: an initial equilibration of 20 ps in which the temperature was elevated gradually from 10 to 300 K during the first 10 ps, followed by a 50 ps of simulation at 300 K for data sampling in which 500 snapshots were recorded at 100 fs intervals. To avoid the "cold solute" problem, temperature scaling was controlled separately for solute and solvent during all the simulations.

Model Evaluation. The conformational validity of main chain and side chain torsions in each residue within the protein models was analyzed using the PROCHECK program.[24] The numbers of exposed hydrophobic or buried polar residues were counted using the ProTable module of SYBYL, where hydrophobic residues (Cys, Phe, Ile, Met, Leu, Val, and Trp) with relative solvent exposure greater than 30% were counted as exposed and polar residues (Asp, Asn, Glu, Gln, Lys, and Arg) with exposure less than 30% as buried according to the default setting of ProTable.

Statistical Analysis of Torsion Angles of Sulfonamide. Using the QUEST3D program,[28] crystal structures of small molecules having the C−N(H)−S(O_2)−C substructure in which the central N−S bond was not in a ring and the carbon on the nitrogen was not involved in a carbonyl or thiocarbonyl group were searched against all entries in the Cambridge Structural Database[28] except for those containing transition metals and those with an *R*-factor greater than 7.5%. As a result, 161 entries were retrieved, from which all the fragments matching the query substructure were further extracted during the QUEST3D search, giving 184 fragments. Distribution of absolute values of C−N−S−C torsion angles in the retrieved fragments was analyzed using the VISTA program,[28] giving the following statistical data: minimum = 45.4°, maximum = 114.8°, mean = 68.8°, SD = 11.5° except for two outliers (146.8° and 178.4°) larger than 120°. Protein−ligand complex crystal structures in which ligand contains the C−N(H)−S(O_2)−C moiety were searched for in the Brookhaven Protein Data Bank[21] through the RELIBase[29] service, providing 16 complexes. Ligand C−N−S−C torsion angles in the retrieved complexes were manually measured with SYBYL and then analyzed, giving the data: minimum = 53.9°, maximum = 98.1°, mean = 71.1°, SD = 11.6° with one outlier of 125.5°.

Chemistry. Melting points were uncorrected. ^{1}H NMR spectra were determined at 200 or 300 MHz. Fast atom bombardment mass spectra (FABMS) and high-resolution (HR)-FABMS were determined using *m*-nitrobenzyl alcohol as a matrix. Unless otherwise stated, all reactions were carried out under a nitrogen atmosphere with anhydrous solvents that had been dried over type 4 Å molecular sieves.

The compounds (**2**, **4**, **5**, **9**, **11**, **13**, and **19**) were prepared and characterized previously by us.[15] All of new compounds (**3**, **6**−**8**, **10**, **12**, **14**−**18**, and **20**−**23**) were also prepared in a similar manner, and their physical, analytical, and spectral data are shown as follows.

(2*R*)-3-Methyl-2-[*N*-methyl[4-(2-phenyl-2*H*-tetrazol-5-yl)phenylsulfonyl]amino]butanoic acid (3):[39] colorless crystals; mp 206−207 °C; $[\alpha]^{22}_D$ +34.8 (*c* 0.5, DMSO); IR (KBr) 3422, 1711, 1336, 1185, 1156 cm^{-1}; ^{1}H NMR (DMSO-d_6) δ 0.95 (d, J = 6.6 Hz, 3H), 0.97 (d, J = 6.6 Hz, 3H), 2.05 (m, 1H), 2.89 (s, 3H), 4.20 (d, J = 10.6 Hz, 1H), 7.52−7.66 (m, 3H), 7.96 (d, J = 8.6 Hz, 2H), 8.16−8.24 (m, 2H), 8.36 (d, J = 8.6 Hz, 2H). Anal. ($C_{19}H_{21}N_5O_4S$) C, H, N, S.

(2*R*)-2-[(4-Bromophenylsulfonyl)amino]-3-phenylpropionic acid (6): colorless crystals; mp 137−138 °C; $[\alpha]^{26}_D$ +3.6° (*c* 0.5, DMSO); IR (KBr) 3343, 1709, 1348, 1170 cm^{-1}; ^{1}H NMR ($CDCl_3$) δ 2.98 (dd, J = 7.0, 13.9 Hz, 1H), 3.15 (dd, J = 5.4, 13.9 Hz, 1H), 4.22 (ddd, J = 5.4, 7.0, 8.9 Hz, 1H), 5.18 (m, 1H), 7.05−7.12 (m, 2H), 7.19−7.29 (m, 3H), 7.52 (s, 4H). Anal. ($C_{15}H_{14}BrNO_4S\cdot0.1H_2O$) C, H, Br, N, S.

(2*R*)-3-Phenyl-2-[[4-(phenylethynyl)phenylsulfonyl]-amino]propionic acid (7): colorless crystals; mp 176−178 °C; $[\alpha]^{24.5}_D$ −9.9° (*c* 0.5, DMSO); IR (KBr) 3427, 3289, 2213, 1721, 1694, 1347, 1163 cm^{-1}; ^{1}H NMR (DMSO-d_6) δ 2.73 (dd, J = 9.3, 13.5 Hz, 1H), 2.96 (dd, J = 5.4, 13.5 Hz, 1H), 3.92 (dt, J = 5.4, 9.3 Hz, 1H), 7.11−7.23 (m, 5H), 7.42−7.50 (m, 3H), 7.52−7.64 (m, 6H), 8.42 (d, J = 9.3 Hz, 1H). Anal. ($C_{23}H_{19}NO_4S$) C, H, N, S.

(2*R*)-3-Phenyl-2-[(*p*-terphenyl-4-ylsulfonyl)amino]propionic acid (8): colorless crystals; mp 224−226 °C; $[\alpha]^{23}_D$ +3.3° (*c* 0.5, DMSO); IR (KBr) 3304, 1750, 1324, 1159 cm^{-1}; ^{1}H NMR (DMSO-d_6) δ 2.75 (dd, J = 9.2, 13.7 Hz, 1H), 2.97 (dd, J = 5.6, 13.7 Hz, 1H), 3.92 (m, 1H), 7.10−7.24 (m, 5H), 7.41 (m, 1H), 7.46−7.58 (m, 2H), 7.60−7.67 (m, 2H), 7.70−7.86 (m, 8H), 8.33 (d, J = 9.2 Hz, 1H). Anal. ($C_{27}H_{23}NO_4S\cdot0.7H_2O$) C, H, N, S.

(2*R*)-3-(1*H*-Indol-3-yl)-2-[[4-[(4-methoxyphenyl)ethynyl]-3-nitrophenylsulfonyl]amino]propionic acid (10): colorless crystals; dec > 200 °C; $[\alpha]^{22}_D$ +5.2° (*c* 0.5, DMSO); IR (KBr) 3444, 2210, 1600, 1513, 1336, 1319, 1171 cm^{-1}; ^{1}H NMR (DMSO-d_6) δ 2.89 (dd, J = 7.8, 14.4 Hz, 1H), 3.15 (dd, J = 3.2, 14.4 Hz, 1H), 3.74 (m, 1H), 3.84 (s, 3H), 6.82−7.11 (m, 7H), 7.19 (d, J = 7.8 Hz, 1H), 7.43 (d, J = 7.8 Hz, 1H), 7.52−7.64 (m, 2H), 7.75 (m, 1H), 8.15 (d, J = 1.4 Hz, 1H), 10.63 (d, J = 1.4 Hz, 1H); HR-FABMS *m*/*z* 518.1024 (M − H)$^-$ (calcd for $C_{26}H_{20}N_3O_7S$ *m*/*z* 518.1022).

(2*R*)-3-(1*H*-Indol-3-yl)-2-[[5-[(3-methylphenyl)ethynyl]-thiophene-2-ylsulfonyl]amino]propionic acid (12): colorless crystals; mp 137−139 °C; $[\alpha]^{25}_D$ +16.7° (*c* 1.0, DMSO); IR (Nujol) 3412, 3336, 2203, 1720, 1340, 1157 cm^{-1}; ^{1}H NMR (DMSO-d_6) δ 2.45 (s, 3H), 2.92 (dd, J = 8.2, 14.5 Hz, 1H), 3.12 (dd, J = 5.8, 14.5 Hz, 1H), 4.00 (dd, J = 5.8, 8.2 Hz, 1H), 6.96 (t, J = 7.4 Hz, 1H), 7.04 (t, J = 7.6 Hz, 1H), 7.11 (d, J = 2.5 Hz, 1H), 7.18 (d, J = 4.0 Hz, 1H), 7.25 (d, J = 4.0 Hz, 1H), 7.27 (dd, J = 2.0, 7.5 Hz, 1H), 7.31 (d, J = 8.1 Hz, 1H), 7.36 (m, 1H), 7.37 (m, 1H), 7.41 (d, J = 7.9 Hz, 1H), 7.54 (d, J = 7.7 Hz, 1H), 8.66 (br s, 1H), 10.84 (s, 1H), 12.86 (br s, 1H). Anal. ($C_{24}H_{20}N_2O_4S_2\cdot0.25H_2O$) C, H, N, S.

(2*R*)-3-(1*H*-Indol-3-yl)-2-[(naphthalen-1-ylsulfonyl)amino]propionic acid (14): colorless foam; $[\alpha]^{23}_D$ −32.9° (*c* 1.0, DMSO); IR (KBr) 3411, 1723, 1593, 1322, 1160, 1132 cm^{-1}; ^{1}H NMR (DMSO-d_6) δ 2.89 (dd, J = 6.6, 14.4 Hz, 1H), 3.07 (dd, J = 6.0, 14.4 Hz, 1H), 3.76 (m, 1H), 6.78−7.05 (m, 3H), 7.18−7.50 (m, 3H), 7.55−7.70 (m, 2H), 7.78−8.23 (m, 4H), 8.59 (m, 1H), 10.66 (s, 1H); HR-FABMS *m*/*z* 393.0908 (M − H)$^-$ (calcd for $C_{21}H_{17}N_2O_4S$ *m*/*z* 393.0909).

(2*R*)-2-[[5-[(4-Ethylphenyl)ethynyl]thiophene-2-ylsulfonyl]amino]-3-(1*H*-indol-3-yl)propionic acid (15): colorless crystals; mp 171−173 °C; $[\alpha]^{22.5}_D$ +21.6° (*c* 1.0, DMSO); IR (KBr) 3431, 3271, 2205, 1713, 1428, 1353, 1161 cm^{-1}; ^{1}H NMR (DMSO-d_6) δ 1.20 (t, J = 7.5 Hz, 3H), 2.66 (q, J = 7.5 Hz, 2H), 2.92 (dd, J = 8.7, 14.1 Hz, 1H), 3.12 (dd, J = 6.0, 14.1 Hz, 1H), 4.01 (m, 1H), 6.97 (m, 1H), 7.05 (m, 1H), 7.11 (d, J = 2.1 Hz, 1H), 7.16 (d, J = 3.9 Hz, 1H), 7.24 (d, J = 3.9 Hz, 1H), 7.31 (d, J = 8.1 Hz, 2H), 7.41 (d, J = 8.1 Hz, 1H), 7.52 (d, J = 8.1 Hz, 2H), 8.67 (d, J = 8.4 Hz, 1H), 10.84 (s, 1H), 12.79 (br s, 1H). Anal. ($C_{25}H_{22}N_2O_4S_2$) C, H, N, S.

(2*R*)-2-[[5-[(4-Butylphenyl)ethynyl]thiophene-2-ylsulfonyl]amino]-3-(1*H*-indol-3-yl)propionic acid (16): colorless crystals; mp 152−154 °C; $[\alpha]^{25}_D$ −13.4° (*c* 0.5, DMSO); IR (KBr) 3412, 3087, 2205, 1737, 1343, 1158 cm^{-1}; ^{1}H NMR (DMSO-d_6) δ 0.90 (t, J = 7.5 Hz, 3H), 1.30 (m, 2H), 1.56 (m, 2H), 2.62 (t, J = 7.5 Hz, 2H), 2.99 (dd, J = 6.6, 14.1 Hz, 1H), 3.14 (dd, J = 5.4, 14.1 Hz, 1H), 3.86 (m, 1H), 6.91−7.12 (m, 3H), 7.20 (d, J = 4.2 Hz, 1H), 7.24−7.34 (m, 4H), 7.44−7.53 (m, 3H), 10.77 (s, 1H); HR-FABMS *m*/*z* 505.1260 (M − H)$^-$ (calcd for $C_{27}H_{25}N_2O_4S_2$ *m*/*z* 505.1256).

(2*R*)-2-[[5-[(4-Butoxyphenyl)ethynyl]thiophene-2-ylsulfonyl]amino]-3-(1*H*-indol-3-yl)propionic acid (17): colorless crystals; mp 174−175 °C; $[\alpha]^{25}_D$ +20.8° (*c* 0.5, DMSO); IR (KBr) 3384, 3287, 2206, 1750, 1335, 1162 cm^{-1}; ^{1}H NMR (DMSO-d_6) δ 0.94 (t, J = 7.5 Hz, 3H), 1.44 (m, 2H), 1.71 (m, 2H), 2.92 (dd, J = 8.4, 14.7 Hz, 1H), 3.11 (dd, J = 5.7, 14.7 Hz, 1H), 3.40 (m, 1H), 4.02 (t, J = 6.6 Hz, 2H), 6.93−7.08 (m, 4H), 7.11 (d, J = 2.4 Hz, 1H), 7.12 (d, J = 3.9 Hz, 1H), 7.23 (d, J = 3.9 Hz, 1H), 7.30−7.43 (m, 2H), 7.49−7.55 (m, 2H), 8.63 (br s, 1H), 10.83 (s, 1H), 12.78 (br s, 1H). Anal. ($C_{27}H_{26}N_2O_5S_2$) C, H, N, S.

(2*R*)-3-(1*H*-Indol-3-yl)-2-[[5-[(4-phenoxyphenyl)ethynyl]-thiophene-2-ylsulfonyl]amino]propionic acid (18): colorless crystals; mp 160−162 °C; $[\alpha]^{26}_D$ −33.7° (*c* 0.5, DMSO); IR (KBr) 3399, 3097, 2205, 1588, 1427, 1242, 1158 cm^{-1}; ^{1}H NMR (DMSO-d_6) δ 3.07 (dd, J = 5.4, 14.1 Hz, 1H), 3.16 (dd, J = 4.5, 14.1 Hz, 1H), 3.71 (m, 1H), 6.90−7.14 (m, 7H), 7.20−7.33 (m, 3H), 7.37−7.49 (m, 3H), 7.51−7.62 (m, 3H), 10.73 (s, 1H); HR-FABMS *m*/*z* 541.0897 (M − H)$^-$ (calcd for $C_{29}H_{21}N_2O_5S_2$ *m*/*z* 541.0892).

(2*R*)-2-[[5-[(4-Ethylphenyl)ethynyl]thiophene-2-ylsulfonyl]amino]-3-methylbutanoic acid (20): colorless crystals; mp 148−149 °C; $[\alpha]^{22.5}_D$ −8.4° (*c* 1.0, DMSO); IR (KBr) 3339, 2965, 2209, 1738, 1378, 1167 cm^{-1}; ^{1}H NMR (DMSO-d_6) δ 0.82 (d, J = 7.0 Hz, 3H), 0.87 (d, J = 6.6 Hz, 3H), 1.19 (t, J = 7.4 Hz, 3H), 1.99 (m, 1H), 2.65 (q, J = 7.4 Hz, 2H), 3.61 (m, 1H), 7.30 (d, J = 8.6 Hz, 2H), 7.39 (d, J = 3.8 Hz, 1H), 7.50 (d, J = 3.8 Hz, 1H), 7.51 (d, J = 8.6 Hz, 2H), 8.47 (d, J = 5.0 Hz, 1H), 12.73 (br s, 1H). Anal. ($C_{19}H_{21}NO_4S_2\cdot0.2H_2O$) C, H, N, S.

(2*R*)-2-[[5-[(4-Butylphenyl)ethynyl]thiophene-2-ylsulfonyl]amino]-3-methylbutanoic acid (21): colorless crystals; mp 147−148 °C; $[\alpha]^{25}_D$ −8.4° (*c* 0.5, DMSO); IR (Nujol) 3329, 2210, 1732, 1355, 1178, 1130 cm^{-1}; ^{1}H NMR (DMSO-d_6) δ 0.82 (d, J = 6.9 Hz, 3H), 0.87 (d, J = 6.9 Hz, 3H), 0.90 (t, J = 7.5 Hz, 3H), 1.30 (m, 2H), 1.56 (m, 2H), 2.00 (m, 1H), 2.62 (t, J = 7.5 Hz, 2H), 3.62 (m, 1H), 7.28 (d, J = 8.4 Hz, 2H), 7.39 (d, J = 3.6 Hz, 1H), 7.47−7.55 (m, 3H), 8.46 (d, J = 8.7 Hz, 1H), 12.74 (br s, 1H). Anal. ($C_{21}H_{25}NO_4S_2$) C, H, N, S.

(2*R*)-2-[[5-[(4-Butoxyphenyl)ethynyl]thiophene-2-ylsulfonyl]amino]-3-methylbutanoic acid (22): colorless crystals; mp 133−134 °C; $[\alpha]^{25}_D$ −8.5° (*c* 0.5, DMSO); IR (KBr) 3330, 2963, 2202, 1732, 1349, 1165 cm^{-1}; ^{1}H NMR (DMSO-d_6) δ 0.82 (d, J = 6.6 Hz, 3H), 0.86 (d, J = 6.9 Hz, 3H), 0.94 (t, J = 7.5 Hz, 3H), 1.43 (m, 2H), 1.71 (m, 2H), 1.99 (m, 1H), 3.60 (m, 1H), 4.02 (t, J = 6.6 Hz, 2H), 6.96−7.04 (m, 2H), 7.35 (d, J = 3.9 Hz, 1H), 7.48 (d, J = 3.9 Hz, 1H), 7.48−7.56 (m, 2H), 8.44 (br s, 1H), 12.73 (br s, 1H). Anal. ($C_{21}H_{25}NO_5S_2$) C, H, N, S.

(2*R*)-3-Methyl-2-[[5-[(4-phenoxyphenyl)ethynyl]thiophene-2-ylsulfonyl]amino]butanoic acid (23): colorless crystals; mp 119−121 °C; $[\alpha]^{26}_D$ −59.8° (*c* 0.5, DMSO); IR (KBr) 3466, 2204, 1588, 1428, 1241, 1158 cm^{-1}; ^{1}H NMR (DMSO-d_6) δ 0.80 (d, J = 7.0 Hz, 3H), 0.87 (d, J = 6.6 Hz, 3H), 2.07 (m,

1H), 3.33 (m, 1H), 6.97−7.14 (m, 4H), 7.22 (m, 1H), 7.35−7.64 (m, 6H); HR-FABMS *m/z* 454.0786 $(M - H)^-$ (calcd for $C_{23}H_{20}NO_5S_2$ *m/z* 454.0783).

MMP-9 and MMP-2 Assays. The inhibitory activity of test compounds to MMP-9 (prepared as described previously[40]) and MMP-2 (purchased from Calbiochem-Novabiochem Corp., La Jolla, CA) was determined by using the synthetic substrate MOCAc-Pro-Leu-Gly-Leu-A_2pr(Dnp)-Ala-Arg-NH_2 (purchased from Peptide Institute, Inc., Osaka, Japan). A mixture of 2 μL of enzyme solution and 1 μL of inhibitor solution was incubated with 46 μL of buffer (50 mM Tris·Cl/10 mM $CaCl_2$/0.2 M NaCl/0.02% (w/v) NaN_3/0.05% (v/v) Brij-35, pH 7.5) at room temperature for 60 min. A 1-μL aliquot of the substrate solution in DMSO (1 mM) was added, and then the reaction was performed for 60 min. After termination of the reaction by addition of 100 μL of 3% aqueous acetic acid, its fluorescence was measured. Excitation and emission wavelengths were 320 and 405 nm, respectively. For each test compound, assays were carried out twice, and then mean value was calculated as inhibitory activity. Standard deviation was not calculated.

Acknowledgment. The authors thank Dr. Yoshikazu Kanbayashi for his helpful discussions throughout this study.

References

(1) Murphy, G. J. P.; Murphy, G.; Reynolds, J. J. The Origin of Matrix Metalloproteinases and Their Familial Relationships. *FEBS Lett.* **1991**, *289*, 4−7.
(2) Birkedal-Hansen, H.; Moor, W. G. I.; Bodden, M. K.; Windsor, L. J.; Birkedal-Hansen, B.; Decarlo, A.; Engler, J. A. Matrix Metalloproteinases: A Review. *Crit. Rev. Oral. Biol. Med.* **1993**, *4*, 197−250.
(3) Cossins, J.; Dudgeon, T. J.; Catlin, G.; Gearing, A. J. H.; Clements, J. M. Identification of MMP-18, a Putative Novel Human Matrix Metalloproteinase. *Biochim. Biophys. Res. Commun.* **1996**, *228*, 494−498.
(4) Pendás, A. M.; Knäuper, V.; Puente, X. S.; Llano, E.; Mattei, M.-G.; Apte, S.; Murphy, G.; López-Otín, C. Identification and Characterization of a Novel Human Matrix Metalloproteinase with Unique Structural Characteristics, Chromosomal Location, and Tissue Distribution. *J. Biol. Chem.* **1997**, *272*, 4281−4286.
(5) Stetler-Stevenson, W. G.; Aznavoorian, S.; Liotta, L. A. Tumor Cell Interactions with the Extracellular Matrix during Invasion and Metastasis. *Annu. Rev. Cell. Biol.* **1993**, *9*, 541−573.
(6) Liotta, L. A.; Steeg, P. S.; Stetler-Stevenson, W. G. Cancer Metastasis and Angiogenesis: An Imbalance of Positive and Negative Regulation. *Cell* **1991**, *64*, 327−336.
(7) Beckett, R. P.; Davidson, A. H.; Drummond, A. H.; Huxley, P.; Whittaker, M. Recent Advances in Matrix Metalloproteinase Inhibitor Research. *Drug Discov. Today* **1996**, *1*, 16−26.
(8) Davidson, A. H.; Drummond, A. H.; Galloway, W. A.; Whittaker, M. The Inhibition of Metalloproteinase Enzymes. *Chem. Ind.* **1997**, 258−261.
(9) (a) Beckett, R. P. Recent Advances in the Field of Matrix Metalloproteinase Inhibitors. *Exp. Opin. Ther. Patents* **1996**, *6*, 1305−1315. (b) Beckett, R. P.; Whittaker, M. Matrix Metalloproteinase Inhibitors 1998. *Exp. Opin. Ther. Patents* **1998**, *8*, 259−282.
(10) Collier, I. E.; Wilhelm, S. M.; Eisen, A. Z.; Marmer, B. L.; Grant, G. A.; Seltzer, J. L.; Kronberger, A.; He, C.; Bauer, E. A.; Goldberg, G. I. H-ras Oncogene-Transformed Human Bronchial Epithelial Cells (TBE-1) Secrete a Single Metalloprotease Capable of Degrading Basement Membrane Collagen. *J. Biol. Chem.* **1988**, *263*, 6579−6587.
(11) Lovejoy, B.; Cleasby, A.; Hassell, A. M.; Longley, K.; Luther, M. A.; Weigl, D.; McGeehan, G.; McElroy, A. B.; Drewry, D.; Lambert, M. H.; Jordan, S. R. Structure of the Catalytic Domain of Fibroblast Collagenase Complexed with an Inhibitor. *Science* **1994**, *263*, 375−377.
(12) Bode, W.; Reinemer, P.; Huber, R.; Kleine, T.; Schnierer, S.; Tschesche, H. The X-ray Crystal Structure of the Catalytic Domain of Human Neutrophil Collagenase Inhibited by a Substrate Analogue Reveals the Essentials for Catalysis and Specificity. *EMBO J.* **1994**, *13*, 1263−1269.
(13) Browner, M. F.; Smith, W. W.; Castelhano, A. L. Matrilysin-Inhibitor Complexes: Common Themes among Metalloproteases. *Biochemistry* **1995**, *34*, 6602−6610.
(14) Gooley, P. R.; O'Connell, J. F.; Marcy, A. I.; Cuca, G. C.; Salowe, S. P.; Bush, B. L.; Hermes, J. D.; Esser, C. K.; Hagmann, W. K.; Springer, J. P.; Johnson, B. A. The NMR Structure of the Inhibited Catalytic Domain of Human Stromelysin-1. *Nature Struct. Biol.* **1994**, *1*, 111−118.
(15) Tamura, Y.; Watanabe, F.; Nakatani, T.; Yasui, K.; Fuji, M.; Komurasaki, T.; Tsuzuki, H.; Maekawa, R.; Yoshioka, T.; Kawada, K.; Sugita, K.; Ohtani, M. Highly Selective and Orally Active Inhibitors of Type IV Collagenase (MMP-9 and MMP-2): *N*-Sulfonylamino Acid Derivatives. *J. Med. Chem.* **1998**, *41*, 640−649.
(16) Paterlini, G.; Portoghese, P. S.; Ferguson, D. M. Molecular Simulation of Dynorphin A-(1−10) Binding to Extracellular Loop 2 of the κ-Opioid Receptor. A Model for Receptor Activation. *J. Med. Chem.* **1997**, *40*, 3254−3262.
(17) Singh, J.; Dobrusin, E. M.; Fry, D. W.; Haske, T.; Whitty, A.; McNamara, D. J. Structure-Based Design of a Potent, Selective, and Irreversible Inhibitor of the Catalytic Domain of the erbB Receptor Subfamily of Protein Tyrosine Kinases. *J. Med. Chem.* **1997**, *40*, 1130−1135.
(18) Costantino, G.; Pellicciari, R. Homology Modeling of Metabotropic Glutamate Receptors. (mGluRs) Structural Motifs Affecting Binding Modes and Pharmacological Profile of mGluR1 Agonists and Competitive Antagonists. *J. Med. Chem.* **1996**, *39*, 3998−4006.
(19) Ferguson, D. M.; Marsh, A. Knowledge-Based Modeling of a Bacterial Dichloromethane Dehalogenase. *Proteins: Struct. Funct. Genet.* **1997**, *28*, 217−226.
(20) Chelvanayagam, G.; Wilce, M. C.; Parker, M. W.; Tan, K. L.; Board, P. G. Homology Model for the Human GSTT2 Theta Class Glutathione Transferase. *Proteins: Struct. Funct. Genet.* **1997**, *27*, 118−130.
(21) Bernstein, F. C.; Koetzle, T. F.; Williams, G. J. B.; Meyer, E. F., Jr.; Brice, M. D.; Rodgers, J. R.; Kennard, O.; Shimanouchi, T.; Tasumi, M. The Protein Data Bank: A Computer-Based Archival File for Macromolecular Structure. *J. Mol. Biol.* **1977**, *112*, 535−542.
(22) Read, R. J.; James, M. N. G. Critical Evaluation of Comparative Model Building of *Streptomyces griseus* Trypsin. *Biochemistry* **1984**, *23*, 6570−6575.
(23) Babine, R. E.; Bender, S. L. Molecular Recognition of Protein−Ligand Complex: Applications to Drug Design. *Chem. Rev.* **1997**, *97*, 1359−1472.
(24) Laskowski, R. A.; MacArthur, M. W.; Moss, D. S.; Thorton, J. PROCHECK: A Program To Check the Stereochemical Quality of Protein Structures. *J. Appl. Crystallogr.* **1993**, *26*, 283−291.
(25) Murtagh, F. A Survey of Recent Advances in Hierarchical Clustering Algorithms. *Comput. J.* **1983**, *26*, 354−359.
(26) Grams, F.; Crimmin, M.; Hinnes, L.; Huxley, P.; Pieper, M.; Tschesche, H.; Bode, W. Structure Determination and Analysis of Human Neutrophil Collagenase Complexed with a Hydroxamate Inhibitor. *Biochemistry* **1995**, *34*, 14012−14020.
(27) Dhanaraj, V.; Ye, Q.-Z.; Johnson, L. L.; Hupe, D. J.; Ortwine, D. F.; Dunbar, J. B., Jr.; Rubin, J. R.; Pavlovsky, A.; Humblet, C.; Blundell, T. L. X-ray Structure of a Hydroxamate Inhibitor Complex of Stromelysin Catalytic Domain and Its Comparison with Members of the Zinc Metalloproteinase Superfamily. *Structure* **1996**, *4*, 375−386.
(28) Cambridge Structural Database System, Ver.5.15; Cambridge Crystallographic Data Centre, 12 Union Rd, Cambridge CB2 1EZ, U.K., 1998.
(29) Free Web-based service that can access receptor/ligand structures deposited in the PDB (http://pdb.pdb.bnl.gov:8081/home-.html).
(30) According to a comment from one of the reviewers, the degree of steric overlap between the thiophene 3,4-positions of compound **11** and the wall of the S1′ pocket was examined. For each atom in the thiophene ring, van der Waals interaction energy with the protein was calculated in each of 500 snapshots during the docking simulation and then statistically analyzed. Similar energy calculation was done for each atom in the corresponding benzene ring of compound **9**. As a result, the hydrogens at the 3,4-positions of the thiophene ring gave negative mean energy values (-2.38 ± 0.26 and -2.42 ± 0.16 kcal/mol), suggesting that there was no severe steric overlap between these positions of the thiophene ring and the wall of the S1′ pocket during the simulation. Interestingly, mean values for the two hydrogens at the corresponding positions on the benzene ring of **9** were less negative (-0.41 ± 0.22 and -0.45 ± 0.27 kcal/mol). Mean vdW energies of whole rings, which were calculated as the sum of the contribution from each ring atom in each snapshot, also showed that the thiophene ring (-13.60 ± 0.82 kcal/mol) of **11** can be accommodated in the S1′ pocket more favorably than the benzene ring (-11.75 ± 1.05 kcal/mol) of **9**. With these calculation results, it was reasonably confirmed that there is no severe steric overlap of the thiophene ring of compound **11** with the wall of the S1′ pocket.
(31) SYBYL 6.4; Tripos, Inc., St. Louis, MO.
(32) Pearlman, D. A.; Case, D. A.; Caldwell, J. C.; Seibel, G. L.; Singh, U. C.; Weiner, P.; Kollman, P. A. AMBER 4.1; University of California, San Francisco, CA.
(33) Stewart, J. J. P. QCPE #455.

(34) Koradi, R.; Billeter, M.; Wüthrich, K. MOLMOL: A Program for Display and Analysis of Macromolecular Structures. *J. Mol. Graph.* **1996**, *14*, 51−55.
(35) GenBank; National Center for Biotechnology Information, National Library of Medicine, Bethesda, MD.
(36) CLUSTAL X: X Window version of CLUSTAL W. Thompson, J. D.; Higgins, D. G.; Gibson, T. J. CLUSTAL W: Improving the Sensitivity of Progressive Multiple Sequence Alignment Through Sequence Weighting, Positions-Specific Gap Penalties and Weight Matrix. *Nucleic Acids Res.* **1994**, *22*, 4673−4680.
(37) Hoops, S. C.; Anderson, K. W.; Merz, K. M., Jr. Force Field Design of Metalloproteins. *J. Am. Chem. Soc.* **1991**, *113*, 8262−8270.
(38) QCPE #429; Connolly, M. L. Solvent-Accessible Surface of Proteins and Nucleic Acids. *Science* **1983**, *221*, 709−713.
(39) Compound **3** was synthesized from the corresponding *tert*-butyl ester using methyl iodide and potassium carbonate in dimethylformamide, followed by trifluoroacetic acid (TFA) hydrolysis.
(40) Ward, R. V.; Hembry, R. M.; Reynolds, J. J.; Murry, G. The Purification of Tissue Inhibitor of Metalloproteinases-2 from Its 72 kDa Progelatinase Complex. *Biochem. J.* **1991**, *278*, 179−187.

JM980514X